

A supermassive black hole in the early universe growing in the shadows

Lukas J. Furtak¹, Ivo Labbé², Adi Zitrin¹, Jenny E. Greene³, Pratika Dayal⁴, Iryna Chemerynska⁵, Vasily Kokorev⁴, Tim B. Miller^{6,7}, Andy D. Goulding³, Rachel Bezanson⁸, Gabriel B. Brammer⁹, Sam E. Cutler¹⁰, Joel Leja^{11,12,13}, Richard Pan¹⁴, Sedona H. Price⁸, Bingjie Wang (王冰洁)^{11,12,13}, John R. Weaver¹⁰, Katherine E. Whitaker^{10,9}, Hakim Atek⁵, Ákos Bogdán¹⁵, Stéphane Charlot⁵, Emma Curtis-Lake¹⁶, Pieter van Dokkum¹⁷, Ryan Endsley¹⁸, Robert Feldmann¹⁹, Yoshinobu Fudamoto^{20,21}, Seiji Fujimoto¹⁸, Anna de Graaff²², Karl Glazebrook², Stéphanie Juneau²³, Danilo Marchesini¹⁴, Michael V. Maseda²⁴, Erica Nelson²⁵, Pascal A. Oesch^{26,9}, Adèle Plat²⁷, David J. Setton⁸, Daniel P. Stark²⁸ and Christina C. Williams^{23,27}

¹*Physics Department, Ben-Gurion University of the Negev, P.O. Box 653, Beer-Sheva 8410501, Israel*

²*Centre for Astrophysics and Supercomputing, Swinburne University of Technology, Melbourne, VIC 3122, Australia*

³*Department of Astrophysical Sciences, Princeton University, 4 Ivy Lane, Princeton, NJ 08544*

⁴*Kapteyn Astronomical Institute, University of Groningen, P.O. Box 800, 9700 AV Groningen, The Netherlands*

⁵*Institut d'Astrophysique de Paris, CNRS, Sorbonne Université, 98bis Boulevard Arago, 75014, Paris, France*

⁶*Department of Astronomy, Yale University, New Haven, CT 06511, USA*

⁷*Center for Interdisciplinary Exploration and Research in Astrophysics (CIERA) and Department*

of Physics and Astronomy, Northwestern University, 1800 Sherman Ave, Evanston IL 60201, USA

⁸*Department of Physics and Astronomy and PITT PACC, University of Pittsburgh, Pittsburgh, PA 15260, USA*

⁹*Cosmic Dawn Center (DAWN), Niels Bohr Institute, University of Copenhagen, Jagtvej 128, København N, DK-2200, Denmark*

¹⁰*Department of Astronomy, University of Massachusetts, Amherst, MA 01003, USA*

¹¹*Department of Astronomy & Astrophysics, The Pennsylvania State University, University Park, PA 16802, USA*

¹²*Institute for Computational & Data Sciences, The Pennsylvania State University, University Park, PA 16802, USA*

¹³*Institute for Gravitation and the Cosmos, The Pennsylvania State University, University Park, PA 16802, USA*

¹⁴*Department of Physics and Astronomy, Tufts University, 574 Boston Ave., Medford, MA 02155, USA*

¹⁵*Center for Astrophysics | Harvard & Smithsonian, 60 Garden Street, Cambridge, MA 02138, USA*

¹⁶*Centre for Astrophysics Research, Department of Physics, Astronomy and Mathematics, University of Hertfordshire, Hatfield AL10 9AB, UK*

¹⁷*Department of Astronomy, Yale University, New Haven, CT 06511, USA*

¹⁸*Department of Astronomy, The University of Texas at Austin, Austin, TX 78712, USA*

¹⁹*Institute for Computational Science, University of Zurich, CH-8057 Zurich, Switzerland*

²⁰Waseda Research Institute for Science and Engineering, Faculty of Science and Engineering, Waseda University, 3-4-1 Okubo, Shinjuku, Tokyo 169-8555, Japan

²¹National Astronomical Observatory of Japan, 2-21-1, Osawa, Mitaka, Tokyo, Japan

²²Max-Planck-Institut für Astronomie, Königstuhl 17, 69117 Heidelberg, Germany

²³NSF's National Optical-Infrared Astronomy Research Laboratory, 950 N. Cherry Avenue, Tucson, AZ 85719, USA

²⁴Department of Astronomy, University of Wisconsin-Madison, 475 N. Charter St., Madison, WI 53706 USA

²⁵Department for Astrophysical and Planetary Science, University of Colorado, Boulder, CO 80309, USA

²⁶Department of Astronomy, University of Geneva, Chemin Pegasi 51, 1290 Versoix, Switzerland

²⁷Steward Observatory, University of Arizona, 933 N Cherry Ave, Tucson, AZ 85721 USA

Early JWST observations have uncovered a new, substantial population of red sources that might represent a previously overlooked phase of actively growing supermassive black holes¹⁻³. One of the most intriguing examples is an extremely red, point-like object that was found to be triply-imaged by the strong lensing galaxy cluster Abell 2744⁴, allowing an unprecedented detailed look into this enigmatic population. Here we present deep spectroscopic JWST/NIRSpec observations of this object, Abell2744-QSO1. The spectroscopy confirms that the three images are of the same object, and that it is a highly reddened ($A_V \sim 3$) broad emission-line Active Galactic Nucleus (AGN) at a redshift of $z_{\text{spec}} = 7.0451 \pm 0.0005$. From the width of $H\beta$ (FWHM = $2800 \pm 250 \frac{\text{km}}{\text{s}}$) we derive a black hole mass of $M_{\text{BH}} =$

$3_{-1}^{+2} \times 10^7 M_{\odot}$. We infer a very high ratio of black hole to galaxy mass of at least 3 % and possibly as high as 100 %, an order of magnitude or more than is seen in local galaxies. The lack of strong metal lines in the spectrum together with the high bolometric luminosity ($L_{\text{bol}} = (1.1 \pm 0.3) \times 10^{45} \frac{\text{erg}}{\text{s}}$) suggest that we are seeing the black hole in a phase of rapid growth, accreting at 30 % of the Eddington limit. Based on early JWST imaging studies we estimate that such heavily reddened, low-mass black holes can be ~ 100 times more common than UV-selected ones at this epoch. The rapid growth and high black hole to galaxy mass ratio of A2744-QSO1 suggests that it may represent the missing link between black hole seeds⁵⁻⁷ and the first luminous quasars⁸.

A2744-QSO1⁴ was discovered in JWST/*Near Infrared Camera*⁹ (NIRCam) pre-imaging from the *Ultra-deep NIRSpect and NIRCam Observations before the Epoch of Reionization*¹⁰ (UNCOVER) program, behind the *Hubble Frontier Fields*¹¹ (HFF) SL cluster Abell 2744¹¹⁻¹⁴ ($z = 0.308$; A2744 hereafter), known to be capable of significantly magnifying distant background objects¹⁵⁻¹⁹. It had been identified as a UV-faint ($M_{\text{UV},1450} = -16.98 \pm 0.09$), lensed high-redshift candidate^{16,20}, but remained an otherwise inconspicuous source in previous $0.5 - 1.5 \mu\text{m}$ observations with the *Hubble Space Telescope* (HST). The NIRCam $1 - 5 \mu\text{m}$ imaging revealed it to be an unusually red ($F277W - F444W = 2.63 \pm 0.10$; $F356W - F444W = 0.83 \pm 0.08$), unresolved point-source triply imaged by the foreground cluster⁴, with the high-redshift nature of the source further supported geometrically by the lensing configuration. A photometric redshift was obtained by modeling the multi-band HST and JWST (F814W, F115W, F150W, F200W, F277W, F356W, F410M, F444W) spectral energy distribution (SED). The unique SED, combined with the point-

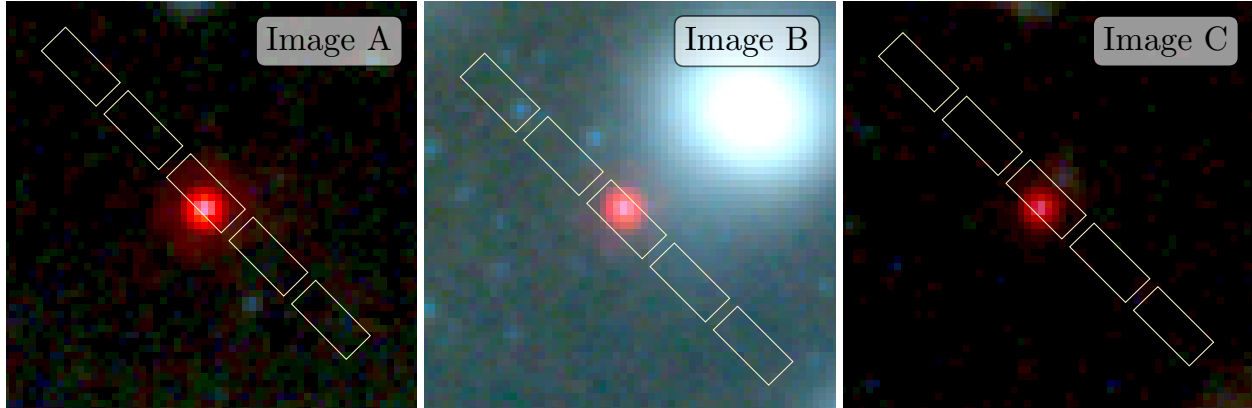


Figure 1: **Composite-color image cutouts of the three images of A2744-QSO1.** The $2.4'' \times 2.4''$ cutouts of the UNCOVER JWST-NIRCam composite-color image¹⁹ (Blue: F115W+F150W, Green: F200W+F277W, Red: F2356W+F410M+F444W) show the three images of A2744-QSO1 overlaid with the NIRSpec MSA slitlets of one of our MSA masks, for example (the three images were targeted with several masks and the exact position of the object in each slit may slightly shift).

like light-profile, hinted that the source may be a highly reddened AGN at redshift $z_{\text{phot}} \simeq 7 - 8^{3,4}$.

The three images of A2744-QSO1 were recently targeted with the *Near Infrared Spectrograph*²¹⁻²³ (NIRSpec) aboard JWST as part of the UNCOVER program (see Fig. 1). The observations were taken July 31 - August 2 2023, using NIRSpec’s multi-shutter array (MSA) mode with the low resolution prism disperser, which covers the wavelength range $0.5 - 5.3 \mu\text{m}$ at spectral resolutions $R \sim 30 - 300$. The exposure times for the three images ranged from 9.3 – 16.4 h. The spectra of three images are stacked to result in one ~ 38 h spectrum, the deepest spectrum so far of any single high-redshift object observed with JWST. After correcting for gravitational magnifications¹⁹ of $\mu_{\text{A}} = 6.2^{+0.5}_{-0.2}$, $\mu_{\text{B}} = 7.3^{+0.1}_{-1.5}$ and $\mu_{\text{C}} = 3.5^{+0.2}_{-0.2}$, this spectrum reaches effective limits up to ~ 31.0 AB at 5σ in the continuum at 1.5 micron, equivalent to integrating for $\gtrsim 1700$ h in a blank field.

The spectrum shown in Fig. 2 features several strong Hydrogen emission lines – a prominent Balmer-series with $H\alpha$, $H\beta$, $H\gamma$ and somewhat weaker $H\delta$, as well as Lyman- α – along with a weak [O III] $\lambda\lambda 4960, 5008\text{\AA}$ -doublet and several faint metal lines. A full list of emission lines is given in Tab. 1. The emission lines securely confirm this object at $z_{\text{spec}} = 7.0451 \pm 0.0005$.

The spectrum provides unambiguous evidence that A2744-QSO1 is an AGN, showing broad emission lines. We measure the emission-line width by fitting a single-component Gaussian to $H\beta$. Note that $H\alpha$ is situated at the very edge of the detector and thus requires more sophisticated modeling (see Methods). For $H\beta$, we find a line-width full-width at half-maximum (FWHM) of $\text{FWHM} = 2800 \pm 250 \frac{\text{km}}{\text{s}}$, well-resolved, even at the relatively low resolution of the prism (see Fig. 2). Such line widths are not seen in star-forming galaxies but routinely observed in the broad-line regions of AGN, where gas clouds orbit the supermassive black hole²⁴. The Balmer emission line ratio ($H\alpha$ to $H\beta$) indicates a strong dust attenuation of $A_V \sim 3$, assuming an SMC extinction law²⁵. Note that flatter attenuation curves yield higher A_V . *Atacama Large Millimeter/submillimeter Array* (ALMA) 1.2 mm observations firmly rule out dusty star formation powering the Balmer lines. If caused by star formation, the emission lines would imply an on-going star-formation rate (SFR) of $\psi \sim 40 \frac{M_\odot}{\text{yr}}$ and a corresponding ~ 1 mJy ALMA 1.2 mm flux, whereas no emission is observed to < 0.1 mJy (at 3σ) in the deep ALMA map.

From the width of the $H\beta$ line (see Fig. 2), we derive the black hole mass M_{BH} . Using standard scaling relations²⁶, we calculate a black hole mass of $M_{\text{BH}} = (3_{-1}^{+2}) \times 10^7 M_\odot$. Note that single-epoch black hole masses are prone to an additional systematic uncertainty of 0.5 dex ²⁷.

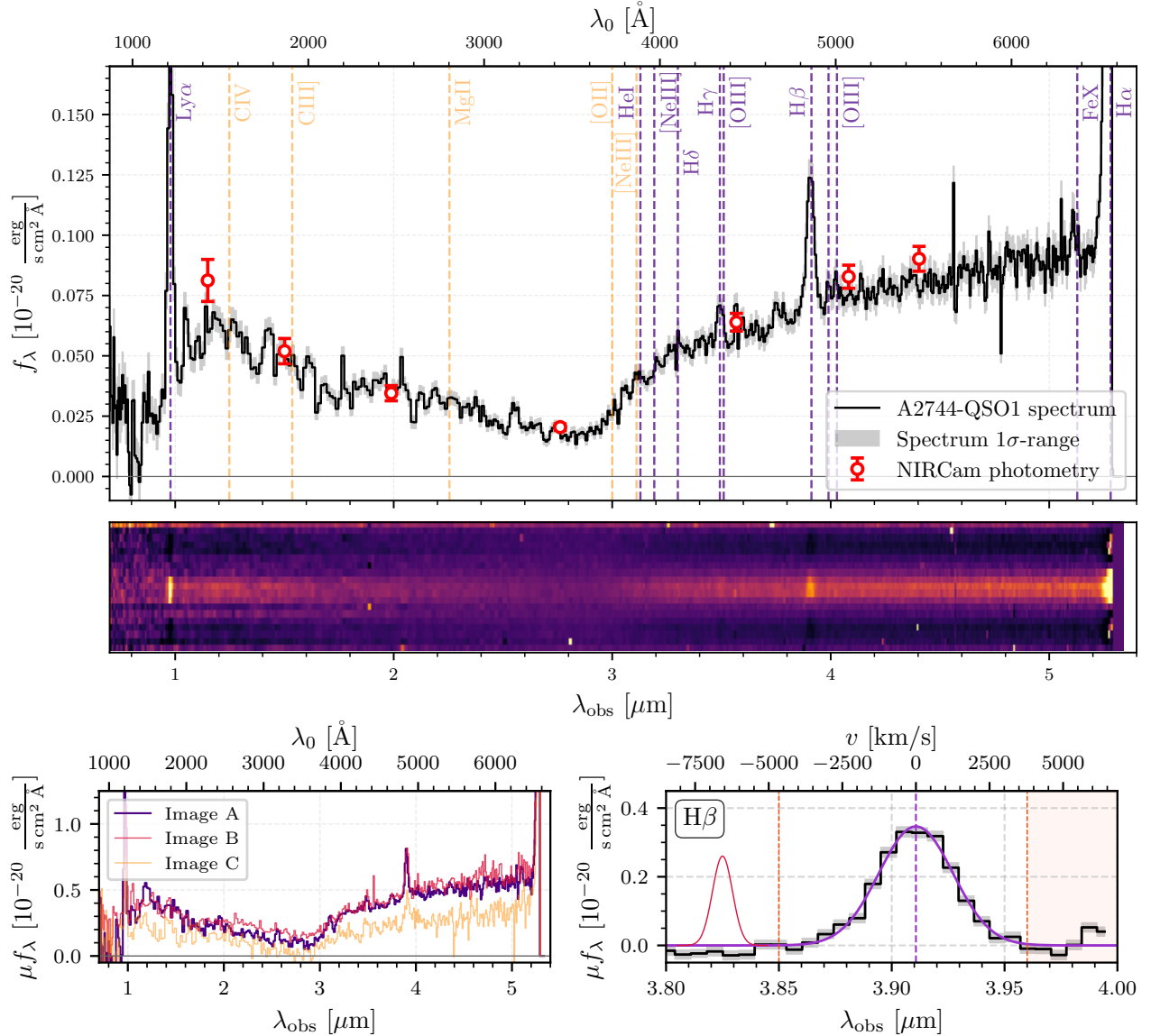


Figure 2: **NIRSpec-prism spectrum of A2744-QSO1.** The *top* panel shows the de-magnified stacked spectrum (black), equivalent to ~ 1700 h integration time on target once the lensing is factored-in, and its 1σ -uncertainty range (grey). In addition to its red rest-frame optical continuum⁴, the source clearly displays strong Hydrogen emission lines in the Balmer-series and Lyman- α . The emission lines allow us to precisely measure the spectroscopic redshift at $z_{\text{spec}} = 7.0451 \pm 0.0005$. We overlay the NIRCам photometry measured previously⁴ as red circles. Securely detected emission lines ($\geq 3\sigma$) are marked in purple and selected non-detected lines are shown in orange. The *bottom left* panel shows the individual (magnified) spectra of the three images. All three images perfectly align in wavelength space, thus confirming the triply-imaged nature of our object. The *bottom right* panel shows the continuum-subtracted $H\beta$ line (black) and our Gaussian fit to the line (purple). The red shaded areas delimit the region in which the fit is performed and the dark red curve illustrates the NIRCам-prism LSF at the wavelength of $H\beta$.

Based on the emission line luminosity, we further derive a bolometric luminosity of $L_{\text{bol}} = (1.1 \pm 0.3) \times 10^{45} \frac{\text{erg}}{\text{s}}$ (see Fig. 3). The black hole must accrete about a tenth of a solar mass per year to maintain this luminosity, which roughly corresponds to 30 % of the Eddington limit – set by the balance between gravity and radiation pressure assuming spherical accretion ($L_{\text{bol}}/L_{\text{Edd}} \sim .3$).

We can also place a limit on the hidden stellar mass of the host galaxy based on the light profile. All three images appear as point-sources, despite different lensing magnifications by a factor 2, which suggests that the intrinsic size of the source is smaller than the point spread function (PSF) of the highest-magnification image. To derive formal upper limits on the size, we fit a Sérsic²⁸ model to the source in the (highest-resolution) F115W-band, finding the source to be unresolved with a size $r_e < 30$ pc (95 % upper limit) after correcting for the lensing shear (equivalent to less than half the size of the PSF). Adopting an upper stellar density limit equal to that of the densest star clusters^{29,30} or the densest elliptical galaxy progenitors^{31,32} known to date, $\Sigma_{\star} \sim 5 \times 10^5 \frac{M_{\odot}}{\text{pc}^2}$, we can then derive an upper limit for how much stellar mass may be contained within $r_e < 30$ pc, thus obtaining $M_{\star} < 1.4 \times 10^9 M_{\odot}$. Our prior photometric fit including ALMA 1.1 mm constraints returns a stellar mass upper limit that is consistent with this estimate³. The implied $M_{\text{BH}} - M_{\star}$ -ratio of $> 3\%$ is extreme compared to local values ($M_{\text{BH}}/M_{\star} \sim 0.1\%$) but similar to some other recently discovered high-redshift black holes^{33,34}.

The spectrum of A2744-QSO1 (Fig. 2) exhibits some distinct characteristics compared to typical AGN³⁵ and other moderate-luminosity $z > 4$ AGN discovered with JWST^{1,36}. The optical continuum is very red, and the metal or high-ionization lines (e.g. the C IV $\lambda\lambda 1548, 1550\text{\AA}$,

Table 1: **Emission lines detected in the combined spectrum of A2744-QSO1.** The stacked spectrum is presented in Fig. 2. Columns represent, from left to right: Emission line designation; rest-frame wavelength; observed wavelength; measured line flux (not corrected for magnification); rest-frame equivalent width. Upper limits are at 3σ . For Lyman- α , the continuum is based on the extrapolated UV assuming a power-law.

Emission Line	λ_0 [Å]	λ_{obs} [μm]	μF_{line} [$10^{-20} \frac{\text{erg}}{\text{s cm}^2}$]	EW_0 [Å]
Ly α	1216	0.978	236.8 ± 18.8	65.5 ± 12.1
Mg II	2796, 2803	2.252	< 11	
He I	3889	3.129	18.3 ± 3.3	
[Ne III]	3968	3.192	15.2 ± 2.5	
H δ	4102	3.300	19.0 ± 2.4	
H γ	4341	3.492	13.6 ± 3.1	
[O III]	4363	3.510	15.3 ± 3.0	
H β	4863	3.912	100.8 ± 3.3	42.5 ± 2.1
[O III]	4960	3.990	5.0 ± 2.6	
[O III]	5008	4.029	15.5 ± 2.6	
[Fe X]	6374	5.128	21.3 ± 3.2	
[N II]	6550	5.270	76.9 ± 19.1	
H α	6565	5.282	753.2 ± 29.1	158.0 ± 11

C III] $\lambda\lambda$ 1907, 1909Å and Mg II $\lambda\lambda$ 2796, 2803Å-doublets in the rest-frame UV, and the [O III] $\lambda\lambda$ 4959, 5007-doublet in the rest-frame optical) are weak compared to the Hydrogen lines (see Fig. 2 and Tab. 1). Furthermore, using the latest 1.25 Ms of X-ray imaging obtained by the *Chandra X-ray Observatory*, we find that all three source images are undetected in X-ray (see Methods). The combined 3σ upper limit on the X-ray luminosity for all three images is $L_{X,2-10} < 3 \times 10^{43} \text{ erg s}^{-1}$, at least $10\times$ weaker than expected based on the UV/optical. This combination of properties strongly suggests that A2744-QSO1 harbors a powerful dusty wind, as are seen in low-mass rapidly accreting black holes at low redshift³⁷, but such dusty wind-dominated sources are very rare at cosmic noon³⁸. In fact, many black holes radiating at or above their Eddington limits display these unique properties^{39,40} perhaps because of changes in the structure of their accretion disk⁴¹. Our estimated Eddington ratio of three is consistent with these characteristics.

A2744-QSO1 represents one of the first examples of a heavily reddened broad-line AGN at such high redshift identified with JWST, although early hints existed also in prior work^{42,43}. These are too UV-faint, however, to have been discovered by past ground-based photometric searches⁴⁴, but many similar compact red objects have been detected in JWST surveys since^{2,3,36}, as well as other high-redshift AGN^{1,36,45-48}, including behind A2744^{34,49}. In fact, another red AGN identified in UNCOVER³ has a spectroscopic redshift of $z = 7.04$, consistent with A2744-QSO1, suggesting these objects may be clustered. Indeed, three out of seven similar objects found in a blank field study² were also at similar redshifts to each other. Nevertheless, A2744-QSO1, remains an important case. As the highest-redshift quasar-like object multiply imaged by a galaxy cluster known to date it affords exquisite signal-to-noise for such a low-luminosity object.

We derive the spatial number density of A2744-QSO1-type objects by taking the sample of “red dots” detected in UNCOVER³ and verifying how many of them are confirmed at the same redshift and UV luminosity with the UNCOVER spectroscopy and updated SL model. This yields a number of two, A2744-QSO1 included, which translates to a number density of $\phi = (7.3 \pm 1.7) \times 10^{-5} \text{ Mpc}^{-3} \text{ mag}^{-1}$. Note that this number density is consistent with what we found based on photometry in UNCOVER³ ($\phi = (2.5_{-2.1}^{+2.6}) \times 10^{-4} \text{ Mpc}^{-3} \text{ mag}^{-1}$) and also with what has been found for reddened $z > 5$ AGN identified in JWST blank fields². While this represents only a few percent of galaxies at this epoch^{50,51}, it is ~ 100 times more numerous than the faintest ground-based UV-selected AGN⁴⁴. Because the UV-luminosity of A2744-QSO1 is only $M_{\text{UV},1450} = -16.98 \pm 0.09$, finding this extremely red point source at high redshifts required the unprecedented infrared-sensitivity of JWST combined with gravitational lensing.

A2744-QSO1 is a significant outlier, both in terms of its $M_{\text{BH}} - M_{\star}$ -ratio (which is still just a lower limit as we do not detect the host galaxy) and the expected number density when compared to theoretical models^{53,54,57}. We use the DELPHI semi-analytic model, that has been shown to reproduce star-forming galaxy luminosity functions at $z \sim 5 - 10$ along with prior AGN luminosity functions. Assuming black hole seeds with a seed mass of $150 M_{\odot}$ originating from metal-free stars, the model predicts that black holes as massive as A2744-QSO1 should be hosted by galaxies with a stellar mass of about $M_{\star} \simeq 10^{10.5} M_{\odot}$ (Fig. 3). The model under-predicts the number density of A2744-QSO1-like objects, and also predicts much lower $M_{\text{BH}} - M_{\star}$ ratios. It is worth noting that hydrodynamic simulations make similar predictions at $z \sim 6^{57,58}$, although typically starting with heavier seeds ($10^{4-6} M_{\odot}$). The models also do not predict the high number density

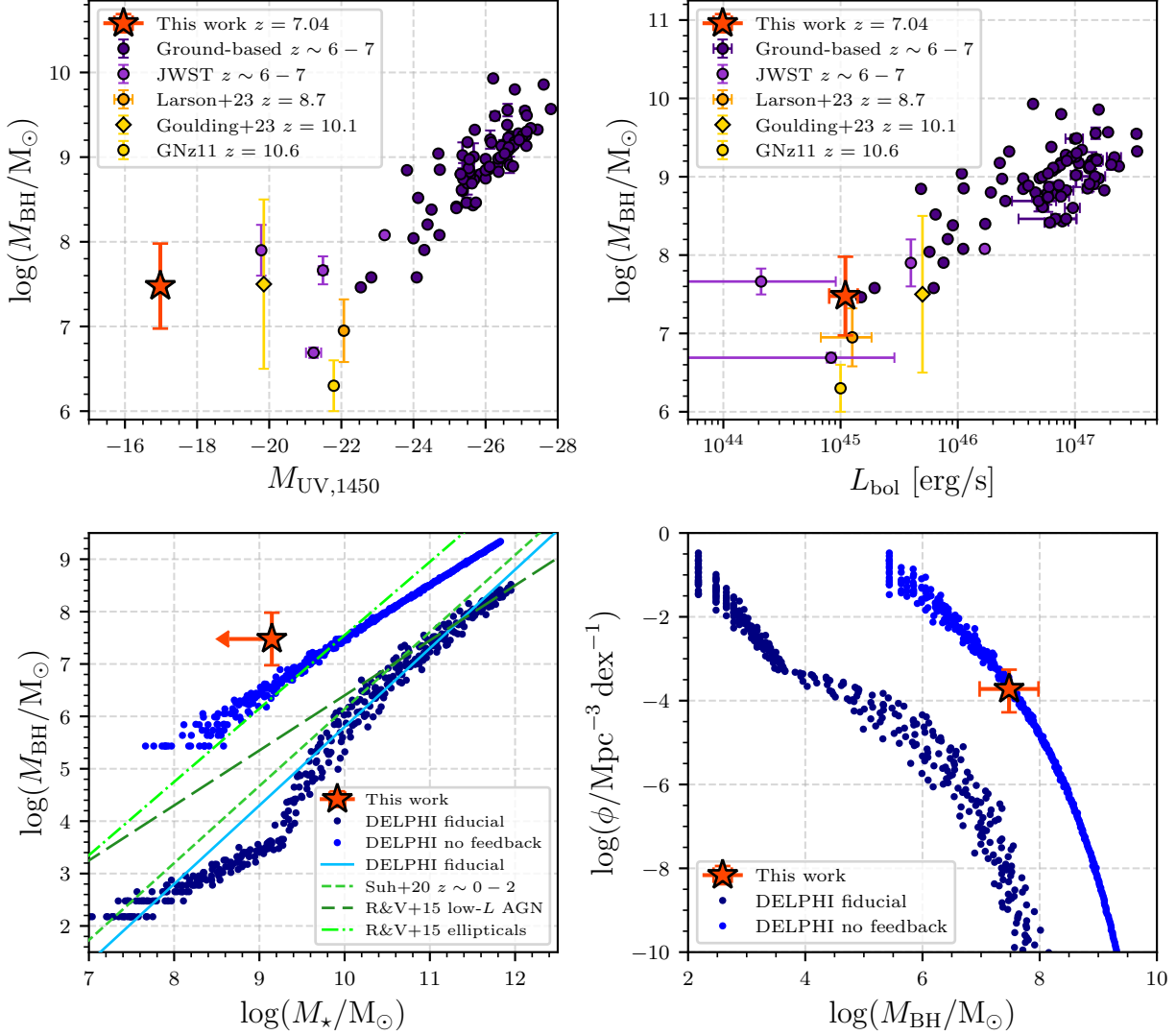


Figure 3: **A2744-QSO1 compared to other broad-line AGN.** The top row shows A2744-QSO1 (red star) in the black hole mass - luminosity space of high-redshift broad-line AGN. Purple circles show UV-bright AGN observed from the ground^{33,52}, the red circles show AGN detected with JWST at $z \sim 6 - 7$ ^{36,42,48}, and the orange and yellow symbols show recently confirmed AGN at higher redshifts^{34,45,47}. A2744-QSO1 is typical in the $M_{\text{BH}} - L_{\text{bol}}$ plane (*top right panel*). In the UV, it is however notably fainter than other AGN recently detected with JWST (*top left panel*), because of the strong dust attenuation. The bottom row shows A2744-QSO1 in $M_{\text{BH}} - M_{\star}$ -space (*bottom left panel*) and in number-densities (*bottom right panel*) compared to the DELPHI simulations^{53,54} (blue) and AGN observed at low redshift^{55,56} (green). The dark blue points show the default DELPHI runs, which predict much higher host stellar masses and much lower number density for a black hole of this mass. The light blue points show the models with feedback turned off, in which case the models can approach the observations of A2744-QSO1.

associated with A2744-QSO1, which can only be reproduced by our extreme model without any feedback (see Fig. 3). This is in conflict with the hints of strong outflows in our source

The discovery of A2744-QSO1 shows that our understanding of black hole growth in the early Universe is still incomplete. The photometric samples suggest high number densities, such that a few percent of galaxies at $z > 7$ harbor reddened and rapidly growing black holes. Deep spectroscopic follow-up with JWST will be needed to confirm these number densities and elucidate their properties. The hints of extreme black hole to galaxy ratios, of a few percent or more, will put strong new constraints on when black holes form relative to their galaxies. There are many outstanding puzzles about these objects remaining that JWST is only beginning to address.

Methods

JWST, ALMA, and Chandra observations The UNCOVER observations used in this work comprise both ultra-deep JWST imaging and spectroscopy of the A2744-field with NIRCcam and NIRSpec to 5σ -depths of 29.9 magnitudes each^{10,59}. Since gravitational magnification on average adds ~ 2 magnitudes to the depth in the SL regime, UNCOVER reaches effective depths of ~ 32 AB once the magnification is factored-in. The NIRCcam data cover a total area of ~ 45 arcmin² in six broad- and one medium-band filter: F115W, F150W, F200W, F277W, F356W, F410M and F444W. The data were reduced and drizzled into mosaics with the `Grism redshift` and `line analysis` software for space-based slitless spectroscopy⁶⁰ (`grizli`; v1.6.0). The UNCOVER mosaics, which also include other public JWST imaging data (i.e. the JWST-GLASS imaging⁶¹ and DDT program 2756; PI: W. Chen) and were made publicly available

on the UNCOVER website¹. The photometry for all three images of A2744-QSO1 can be found in Table 1 of the discovery paper for A2744-QSO1⁴.

The NIRSpec component of the UNCOVER survey consists of seven micro-shutter array (MSA) pointings on the A2744-field with various exposure times between ~ 3 h and ~ 17 h, totalling 24 h NIRSpec time and 680 targeted objects. The observations follow a 2-point dither pattern and a 3-shutter slit-let nod pattern at a position angle of 266° . We use the NIRSpec-prism as dispersion element, thus achieving spectral resolutions of $R \sim 30-300$ in wavelengths spanning $0.6-5.3 \mu\text{m}$. The prism data were reduced with `MSAEXP`⁶² (v0.6.10). The code works on individual frames to correct for $1/f$ -noise, find and mask snowballs, and remove the bias. The pipeline first applies a WCS, and then identifies each slit and applies the flat-fielding and photometric corrections. The 2D-slits are then extracted and drizzled onto a common grid. The details of the observational setup and reduced data products, planned for public release before JWST Cycle 3, will be presented in Price et al. (in prep.). All three images of A2744-QSO1 were included in the MSA designs with cumulated exposure times 17.4 h, 9.9 h and 14.7 h for images A, B and C respectively.

In addition, A2744 is part of the *ALMA Frontier Fields* survey⁶³, which obtained first deep 1.1 mm imaging of the cluster core. These data have now recently been complemented with additional observations covering the entire UNCOVER footprint (Program ID: 2022.1.00073.S; PI: S. Fujimoto), achieving 1σ depths down to $32.7 \mu\text{Jy}/\text{beam}$ over an area of $\sim 24 \text{ arcmin}^2$. The UNCOVER ALMA data will also be publicly released shortly in Fujimoto et al. (in prep).

¹<https://jwst-uncover.github.io/DR1.html#Mosaics>

A2744 has also been the subject of sensitive X-ray follow-up observations using the *Chandra X-ray observatory* (PI: A. Bogdan). The 1.25 Ms of *Chandra* ACIS data used here was previously reduced, analyzed and presented in the supplementary materials section of Bogdan et al.⁴⁹. We use these data products to perform forced photometry at the locations of the three images of A2744-QSO1. Images A and B are heavily contaminated by the foreground X-ray gas associated with A2744 itself. Image C provides the cleanest (lowest-background) region to perform an X-ray analysis of A2744-QSO1, however, we find no significant detection of an X-ray point source. We place a 3σ upper limit of < 12.8 photons in the 2 – 7 keV energy band, i.e. a flux limit of $f_{X,2-10\text{keV}} < 2.8 \times 10^{-16} \frac{\text{erg}}{\text{scm}^2}$ assuming a typical AGN X-ray power-law slope of $\Gamma = 1.9$, equivalent to a de-magnified X-ray luminosity of $L_{X,2-10\text{keV}} < 5 \times 10^{43} \frac{\text{erg}}{\text{s}}$ at the redshift of A2744-QSO1. Stacking and de-magnifying all three images produces a marginal increase in sensitivity, owing to the increased magnification but higher backgrounds of images A and B of $L_{X,2-10\text{keV}} < 3 \times 10^{43} \frac{\text{erg}}{\text{s}}$.

Gravitational lensing Throughout this work we use the most recent SL model of A2744 by Furtak et al.¹⁹, which is based on UNCOVER data and publicly available². The model is slightly updated here with one new multiple image system and an additional spectroscopic redshift¹⁸. The model was constructed using a new implementation of the Zitrin-parametric code^{19,64,65}, which is not coupled to a fixed grid resolution and thus capable of high resolution results. For the model, the cluster galaxies are modeled each as a double Pseudo Isothermal Ellipsoid⁶⁶ (dPIE), scaled

²Version v1.1 of the UNCOVER lens model: <https://jwst-uncover.github.io/DR1.html#LensingMaps>.

according to its luminosity using common scaling relations motivated by the fundamental plane. Three of the brightest cluster galaxies (BCGs), as well as several other galaxies situated close to multiple images, are modeled independently. We use 421 cluster galaxies throughout the UNCOVER $\sim 45 \text{ arcmin}^2$ field-of-view, more than half of which are spectroscopically confirmed¹⁷. The rest were chosen based on the cluster’s red-sequence, identified in a color-magnitude diagram based on the HST/ACS F606W- and F814W-bands bracketing their 4000 Å-break. Five cluster-scale dark matter (DM) halos are employed, each modeled as a pseudo isothermal elliptical mass distribution^{67,68} (PIEMD). These DM halos are centered on the five BCGs but for three of them, the central position can be iterated for in the minimization process within a couple of arc-seconds around their respective BCG’s position. As constraints, 141 multiple images (belonging to 48 sources) are used, 96 of which have spectroscopic redshifts. The vast majority of these is situated in the main cluster core just like A2744-QSO1. The minimization is performed in the source plane using a $\sim 10^5$ -step MCMC process. For the minimization and uncertainty estimation, we use a positional uncertainty of 0.5” for each multiple image. The resulting model has a very good image reproduction RMS of $\Delta_{\text{RMS}} = 0.51$ ” in the lens plane. We infer magnifications and 95% confidence intervals of $\mu_{\text{A}} = 6.15 [5.76, 6.92]$, $\mu_{\text{B}} = 7.29 [5.11, 7.65]$ and $\mu_{\text{C}} = 3.55 [3.31, 3.80]$ for images A, B and C respectively. These are only very slightly different from the magnifications presented in Furtak et al.⁴ and are in generally good agreement with the photometric flux ratios.

Spectroscopic analysis We use the image multiplicity of A2744-QSO1 to achieve maximum signal-to-noise by stacking the weighted, local-background subtracted and co-added spectra of the three images. The spectrum is then extracted with MSAEXP using an optimal extraction⁶⁹

and collapsed to a 1D-spectrum. Taking the magnification into account, the effective exposure time of this stacked spectrum is of about 1700 h. The flux-calibration is then performed by bootstrapping to the total photometry of image A, which has the cleanest photometric measurement⁴. Wavelength-dependent corrections are modeled with a first-order polynomial.

The final stacked spectrum of A2744-QSO1 displays numerous emission lines and is shown in Fig. 2. For the most robust emission line in our spectrum, the Balmer line $H\beta$, we use `specutils`⁷⁰ (v1.10.0) to fit a Gaussian profile to the continuum-subtracted emission line and estimate the uncertainties with an MCMC-analysis using `emcee`⁷¹ (v3.1.4). Our line-fit explicitly includes the NIRSpec line-spread-function (LSF) into the model at the wavelength of $H\beta$. The $\text{FWHM} = 2800 \pm 250 \frac{\text{km}}{\text{s}}$ used in the following is therefore intrinsic, i.e. corrected for instrumental effects. $H\alpha$ is more challenging to model as the red wing of the spectrum falls off the detector and it is blended with $[\text{N II}] \lambda\lambda 6550, 6585\text{\AA}$. In addition, the line profile appears to show a narrow component on top of the broad wing, which is not well described by a single Gaussian. For completeness, we therefore proceed to model $H\alpha$, $[\text{N II}] \lambda\lambda 6550$, $H\beta$, and $[\text{O III}]$ jointly, fixing the metal lines to $100 \frac{\text{km}}{\text{s}}$ FWHM, restricting the narrow-to-broad line ratio to be the same for $H\beta$ and $H\alpha$, but allowing for different line widths between $H\beta$, and $H\alpha$. Encouragingly, the fit parameters are well constrained and reproduce the single-Gaussian broad line width of $H\beta$, while finding a smaller FWHM for the broad component of $H\alpha$ $\text{FWHM} \simeq 2300 \pm 250 \frac{\text{km}}{\text{s}}$ as is commonly seen in low redshift AGN²⁶. Other spectral lines are identified and modeled with single Gaussians and presented in Tab. 1.

We derive a Balmer decrement of 7.4 ± 0.4 from the Balmer line measurements in Tab. 1.

Assuming an reddening law based on fits to the Small Magellanic Cloud²⁵ (SMC) and for $R_V = 2.72^{72,73}$ we find $A_V = 3$, $A(H\beta) = 3.1$, and $A(H\alpha) = 2.1$. The line fluxes are corrected for this high level of attenuation before black hole mass and Eddington ratio calculations are made. We note that if we assumed a flatter reddening law⁷⁴, the reddening corrections would be larger as would the bolometric luminosity⁷⁵. While the Balmer decrement in the broad-line region arises in part within the broad-line region itself⁷⁶, we note that we derive very comparable A_V from the photometric modeling^{3,4}.

To investigate a possible SFR origin of the Balmer lines, we convert the dust-corrected $H\alpha$ luminosity to an SFR⁷⁷, resulting in an on-going SFR $\psi \sim 40 \frac{M_\odot}{\text{yr}}$ and predict the infrared fluxes using the Flexible Stellar Population Synthesis code⁷⁸, which implements the Draine & Li² dust model. The predicted ALMA 1.2 mm fluxes are $f_{1.2\text{mm}} \sim 1$ mJy in contrast with a 3σ upper limit of < 0.1 mJy based on the deep ALMA map.

We use the $H\beta$ and $H\alpha$ line widths and attenuation-corrected line fluxes to estimate the single-epoch black hole mass. Because we do not measure the intrinsic continuum, we use the dereddened Balmer line luminosity to calculate M_{BH}^{26} . We find a black hole mass of $M_{\text{BH}} = (3_{-1}^{+2}) \times 10^7 M_\odot$, taking the average of $H\alpha$ and $H\beta$, which are consistent with each. The errors reflect both line width uncertainty and differences between $H\alpha$ and $H\beta$ that may result from systematic effects like reddening corrections. The additional systematic uncertainty term on single-epoch black hole masses is estimated to be ~ 0.5 dex²⁷. We find a bolometric luminosity of $1.1 \pm 0.3 \times 10^{45}$ erg s⁻¹, assuming a bolometric correction of 10 ± 2 ⁷⁹. The continuum luminosity estimated in⁴ is higher than this estimate by nearly a factor of ten, resulting from uncertainties in

quantities like the redshift and the reddening. We thus infer an Eddington ratio of $L_{\text{bol}}/L_{\text{Edd}} \approx 0.3$.

Size measurement Furtak et al.⁴ used `galfit`⁸⁰ measurements to the individual images of A2744-QSO1, in all available broad bands from F115W to F444W, together with the fact that all three images appear as point sources despite suffering different amounts of shear and magnification, to conclude that the object was indeed point-like and from the PSF size to obtain a source size estimate of $r_e < 35 \text{ pc}$.

Here we revisit this size estimate with the most up-to-date PSF models and data reduction. Using `pysersic`⁸¹, we fit a single Sérsic model to the F150W image. We find a firm upper limit on the size of $r_e < 11.2_{-0.8}^{+1.6}$ milli-arcseconds, which translates to a 2σ upper limit of $r_e \lesssim 100 \text{ pc}$ for the lensed image. Applying a lensing correction of $\mu_t = 3.52$ – the tangential shear in the most magnified image – we then confirm a firm 2σ upper limit of 30 pc on the source radius, in agreement with the Furtak et al. measurement⁴.

Number density In order to derive the number density of objects like A2744-QSO1, it is needed to compute the corresponding effective co-moving volume V_{eff} which folds-in the lensing distortion and possible selection effects. This is done following a forward-modeling approach⁵¹, the detailed procedure of which will be published in Chemerynska et al. (in prep.): We use the (de-magnified) SED of A2744-QSO1 to populate the UNCOVER source plane of A2744¹⁹ with 10000 similar mock sources. These are then deflected into the lens plane and injected in the UNCOVER mosaics on which we re-run the source detection and selection methods used for the catalogs^{59,82}. The ratio of recovered to injected sources allows us to determine the selection-function for objects such as

A2744-QSO1. This selection-function is multiplied with the co-moving volume element which is then integrated over the source-plane area of sufficient magnification that allows us to detect the source at 3σ in each NIRC*am* band, given the UNCOVER mosaic depths⁵⁹. The thus obtained effective volume for A2744-QSO1 is $V_{\text{eff}} = 27541 \pm 294 \text{ Mpc}^3$.

Given that the $\sim 45 \text{ arcmin}^2$ of the UNCOVER field-of-view¹⁰ contains two “red dot” objects of the redshift and UV luminosity of A2744-QSO1³, A2744-QSO1 itself and one other (Greene et al., in prep.) projected 369 kpc away in the source plane, the number density is $\phi = (7.3 \pm 1.7) \times 10^{-5} \text{ Mpc}^{-3} \text{ mag}^{-1}$.

Theoretical expectation We compare our results to the `Dark matter and the Emergence of galaxies in the ePoch of reIonization`^{53,54} (DELPHI) semi-analytic model. This is suited to jointly track the assembly of the dark matter, baryonic and black hole components of high-redshift ($z \gtrsim 7$) galaxies up to $z \sim 40$. Starting at $z \sim 7$, we build analytic (binary) merger trees for 700 galaxies equally spaced in log-space in the halo mass range $M_{\text{h}} = 10^8 - 10^{15} M_{\odot}$ using a constant time-step of 30 Myr. Each of these halos is assigned a number density according to the Sheth-Tormen halo mass function⁸³ at $z \sim 7$ and the number density propagated throughout the merger tree.

In this work, we only consider seeding by stellar black hole seeds formed from metal-free (Pop. III) stars. The first halos (starting leaves) of any halo are seeded with a stellar black hole (of $150 M_{\odot}$) at $z > 13$ assuming that halos collapsing from high ($\gtrsim 3.5$)- σ fluctuations in the primordial density field are most likely to host such seeds. At any time-step, the initial gas mass is the sum

of that brought-in by mergers and smooth accretion. A fraction of this gas can form stars with an efficiency that is the minimum between the Supernovae (SN II) energy required to unbind the rest of the gas and an upper threshold f_* . In terms of black holes, in our *fiducial* model, these grow both through (instantaneous) mergers and accretion. A fraction of the gas mass left in the halo after star formation and its associated feedback can be accreted onto the black hole with the accretion rate depending on a critical halo mass (which at $z \sim 7$ corresponds to $10^{10.9} M_\odot$). While black holes in lower mass halos are assumed to have puffed-up disks, only allowing for low accretion rates ($\sim 7.5 \times 10^{-5}$ Eddington), black holes in halos above this critical mass can accrete a fixed fraction of the gas mass up to the Eddington limit; a fraction of the black hole energy (0.3 %) is allowed to couple to the gas content. The *maximal (no feedback)* model presents an upper limit where every black hole is always allowed to accrete the gas mass available, up to the Eddington limit and we ignore gas mass lost in outflows, both due to SN II and black hole feedback.

The model has been tuned to reproduce all the key observables for both star-forming galaxies at $z \sim 5-10$ (including the evolving UV luminosity and stellar mass functions) and AGN at $z \sim 5-6$ (including the AGN UV luminosity and black hole mass functions).

1. Kocevski, D. D. *et al.* Hidden Little Monsters: Spectroscopic Identification of Low-Mass, Broad-Line AGN at $z > 5$ with CEERS. *arXiv e-prints* arXiv:2302.00012 (2023).
2. Matthee, J. *et al.* Little Red Dots: an abundant population of faint AGN at $z \sim 5$ revealed by the EIGER and FRESCO JWST surveys. *arXiv e-prints* arXiv:2306.05448 (2023).
3. Labbe, I. *et al.* UNCOVER: Candidate Red Active Galactic Nuclei at $3 < z < 7$ with JWST

- and ALMA. *arXiv e-prints* arXiv:2306.07320 (2023).
4. Furtak, L. J. *et al.* JWST UNCOVER: Extremely Red and Compact Object at $z_{\text{phot}} \simeq 7.6$ Triply Imaged by A2744. *ApJ* **952**, 142 (2023).
 5. Inayoshi, K., Visbal, E. & Haiman, Z. The Assembly of the First Massive Black Holes. *ARA&A* **58**, 27–97 (2020).
 6. Greene, J. E., Strader, J. & Ho, L. C. Intermediate-Mass Black Holes. *ARA&A* **58**, 257–312 (2020).
 7. Volonteri, M., Habouzit, M. & Colpi, M. The origins of massive black holes. *Nature Reviews Physics* **3**, 732–743 (2021).
 8. Fan, X., Banados, E. & Simcoe, R. A. Quasars and the Intergalactic Medium at Cosmic Dawn. *arXiv e-prints* arXiv:2212.06907 (2022).
 9. Rieke, M. J. *et al.* Performance of NIRCcam on JWST in Flight. *PASP* **135**, 028001 (2023).
 10. Bezanson, R. *et al.* The JWST UNCOVER Treasury survey: Ultradeep NIRSspec and NIRCcam Observations before the Epoch of Reionization. *arXiv e-prints* arXiv:2212.04026 (2022).
 11. Lotz, J. M. *et al.* The Frontier Fields: Survey Design and Initial Results. *ApJ* **837**, 97 (2017).
 12. Abell, G. O., Corwin, H. G., Jr. & Olowin, R. P. A catalog of rich clusters of galaxies. *ApJS* **70**, 1–138 (1989).
 13. Allen, S. W. Resolving the discrepancy between X-ray and gravitational lensing mass measurements for clusters of galaxies. *MNRAS* **296**, 392–406 (1998).

14. Ebeling, H. *et al.* The X-ray brightest clusters of galaxies from the Massive Cluster Survey. *MNRAS* **407**, 83–93 (2010).
15. Merten, J. *et al.* Creation of cosmic structure in the complex galaxy cluster merger Abell 2744. *MNRAS* **417**, 333–347 (2011).
16. Mahler, G. *et al.* Strong-lensing analysis of A2744 with MUSE and Hubble Frontier Fields images. *MNRAS* **473**, 663–692 (2018).
17. Bergamini, P. *et al.* New high-precision strong lensing modeling of Abell 2744. Preparing for JWST observations. *A&A* **670**, A60 (2023).
18. Bergamini, P. *et al.* The GLASS-JWST Early Release Science Program. III. Strong-lensing Model of Abell 2744 and Its Infalling Regions. *ApJ* **952**, 84 (2023).
19. Furtak, L. J. *et al.* UNCOVERing the extended strong lensing structures of Abell 2744 with the deepest JWST imaging. *MNRAS* **523**, 4568–4582 (2023).
20. Atek, H. *et al.* Probing the $z > 6$ Universe with the First Hubble Frontier Fields Cluster A2744. *ApJ* **786**, 60 (2014).
21. Jakobsen, P. *et al.* The Near-Infrared Spectrograph (NIRSpec) on the James Webb Space Telescope. I. Overview of the instrument and its capabilities. *A&A* **661**, A80 (2022).
22. Böker, T. *et al.* In-orbit Performance of the Near-infrared Spectrograph NIRSpec on the James Webb Space Telescope. *PASP* **135**, 038001 (2023).

23. Ferruit, P. *et al.* The Near-Infrared Spectrograph (NIRSpec) on the James Webb Space Telescope. II. Multi-object spectroscopy (MOS). *A&A* **661**, A81 (2022).
24. Hao, L. *et al.* Active Galactic Nuclei in the Sloan Digital Sky Survey. II. Emission-Line Luminosity Function. *AJ* **129**, 1795–1808 (2005).
25. Gordon, K. D., Clayton, G. C., Misselt, K. A., Landolt, A. U. & Wolff, M. J. A Quantitative Comparison of the Small Magellanic Cloud, Large Magellanic Cloud, and Milky Way Ultraviolet to Near-Infrared Extinction Curves. *ApJ* **594**, 279–293 (2003).
26. Greene, J. E. & Ho, L. C. Estimating Black Hole Masses in Active Galaxies Using the H α Emission Line. *ApJ* **630**, 122–129 (2005).
27. Shen, Y. The mass of quasars. *Bulletin of the Astronomical Society of India* **41**, 61–115 (2013).
28. Sérsic, J. L. Influence of the atmospheric and instrumental dispersion on the brightness distribution in a galaxy. *Boletín de la Asociación Argentina de Astronomía La Plata Argentina* **6**, 41–43 (1963).
29. Norris, M. A. *et al.* The AIMSS Project - I. Bridging the star cluster-galaxy divide. *MNRAS* **443**, 1151–1172 (2014).
30. Vanzella, E. *et al.* JWST/NIRCam Probes Young Star Clusters in the Reionization Era Sunrise Arc. *ApJ* **945**, 53 (2023).

31. Bezanson, R. *et al.* The Relation Between Compact, Quiescent High-redshift Galaxies and Massive Nearby Elliptical Galaxies: Evidence for Hierarchical, Inside-Out Growth. *ApJ* **697**, 1290–1298 (2009).
32. Baggen, J. F. W. *et al.* Sizes and mass profiles of candidate massive galaxies discovered by JWST at $7 < z < 9$: evidence for very early formation of the central ~ 100 pc of present-day ellipticals. *arXiv e-prints* arXiv:2305.17162 (2023).
33. Izumi, T. *et al.* Subaru High- z Exploration of Low-luminosity Quasars (SHELLQs). XIII. Large-scale Feedback and Star Formation in a Low-luminosity Quasar at $z = 7.07$ on the Local Black Hole to Host Mass Relation. *ApJ* **914**, 36 (2021).
34. Goulding, A. D. *et al.* UNCOVER: The growth of the first massive black holes from JWST/NIRSpec – spectroscopic confirmation of an X-ray luminous AGN at $z=10.1$. *arXiv e-prints* arXiv:2308.02750 (2023).
35. Vanden Berk, D. E. *et al.* Composite Quasar Spectra from the Sloan Digital Sky Survey. *AJ* **122**, 549–564 (2001).
36. Harikane, Y. *et al.* JWST/NIRSpec First Census of Broad-Line AGNs at $z=4-7$: Detection of 10 Faint AGNs with $M_{\text{BH}} \sim 10^6 - 10^7 M_{\odot}$ and Their Host Galaxy Properties. *arXiv e-prints* arXiv:2303.11946 (2023).
37. Veilleux, S., Meléndez, M., Tripp, T. M., Hamann, F. & Rupke, D. S. N. The Complete Ultraviolet Spectrum of the Archetypal “Wind-dominated” Quasar Mrk 231: Absorption and Emission from a High-speed Dusty Nuclear Outflow. *ApJ* **825**, 42 (2016).

38. Zakamska, N. L. *et al.* Discovery of extreme [O III] $\lambda 5007$ Å outflows in high-redshift red quasars. *MNRAS* **459**, 3144–3160 (2016).
39. Osterbrock, D. E. & Pogge, R. W. The spectra of narrow-line Seyfert 1 galaxies. *ApJ* **297**, 166–176 (1985).
40. Leighly, K. M., Halpern, J. P., Jenkins, E. B. & Casebeer, D. The Intrinsically X-Ray-weak Quasar PHL 1811. II. Optical and UV Spectra and Analysis. *ApJS* **173**, 1–36 (2007).
41. Abramowicz, M. A., Czerny, B., Lasota, J. P. & Szuszkiewicz, E. Slim Accretion Disks. *ApJ* **332**, 646 (1988).
42. Fujimoto, S. *et al.* A dusty compact object bridging galaxies and quasars at cosmic dawn. *Nature* **604**, 261–265 (2022).
43. Endsley, R. *et al.* ALMA confirmation of an obscured hyperluminous radio-loud AGN at $z = 6.853$ associated with a dusty starburst in the 1.5 deg² COSMOS field. *MNRAS* **520**, 4609–4620 (2023).
44. Matsuoka, Y. *et al.* Quasar Luminosity Function at $z = 7$. *ApJ* **949**, L42 (2023).
45. Larson, R. L. *et al.* A CEERS Discovery of an Accreting Supermassive Black Hole 570 Myr after the Big Bang: Identifying a Progenitor of Massive $z > 6$ Quasars. *arXiv e-prints* arXiv:2303.08918 (2023).
46. Barro, G. *et al.* Extremely red galaxies at $z = 5 - 9$ with MIRI and NIRSpec: dusty galaxies or obscured AGNs? *arXiv e-prints* arXiv:2305.14418 (2023).

47. Maiolino, R. *et al.* A small and vigorous black hole in the early Universe. *arXiv e-prints* arXiv:2305.12492 (2023).
48. Maiolino, R. *et al.* JADES. The diverse population of infant Black Holes at $4 < z < 11$: merging, tiny, poor, but mighty. *arXiv e-prints* arXiv:2308.01230 (2023).
49. Bogdan, A. *et al.* Detection of an X-ray quasar in a gravitationally-lensed $z=10.3$ galaxy suggests that early supermassive black holes originate from heavy seeds. *arXiv e-prints* arXiv:2305.15458 (2023).
50. Bouwens, R. J., Oesch, P. A., Illingworth, G. D., Ellis, R. S. & Stefanon, M. The $z \sim 6$ Luminosity Function Fainter than -15 mag from the Hubble Frontier Fields: The Impact of Magnification Uncertainties. *ApJ* **843**, 129 (2017).
51. Atek, H., Richard, J., Kneib, J.-P. & Schaerer, D. The extreme faint end of the UV luminosity function at $z \sim 6$ through gravitational telescopes: a comprehensive assessment of strong lensing uncertainties. *MNRAS* **479**, 5184–5195 (2018).
52. Yang, J. *et al.* Probing early supermassive black hole growth and quasar evolution with near-infrared spectroscopy of 37 reionization-era quasars at $6.3 \leq z \leq 7.64$. *The Astrophysical Journal* **923**, 262 (2021). URL <https://dx.doi.org/10.3847/1538-4357/ac2b32>.
53. Dayal, P. *et al.* The hierarchical assembly of galaxies and black holes in the first billion years: predictions for the era of gravitational wave astronomy. *MNRAS* **486**, 2336–2350 (2019).
54. Piana, O., Dayal, P., Volonteri, M. & Choudhury, T. R. The mass assembly of high-redshift black holes. *MNRAS* **500**, 2146–2158 (2021).

55. Reines, A. E. & Volonteri, M. Relations between Central Black Hole Mass and Total Galaxy Stellar Mass in the Local Universe. *ApJ* **813**, 82 (2015).
56. Suh, H. *et al.* No Significant Evolution of Relations between Black Hole Mass and Galaxy Total Stellar Mass Up to $z \sim 2.5$. *ApJ* **889**, 32 (2020).
57. Habouzit, M. *et al.* Co-evolution of massive black holes and their host galaxies at high redshift: discrepancies from six cosmological simulations and the key role of JWST. *MNRAS* **511**, 3751–3767 (2022).
58. Çatmabacak, O. *et al.* Black hole-galaxy scaling relations in FIRE: the importance of black hole location and mergers. *MNRAS* **511**, 506–535 (2022).
59. Weaver, J. R. *et al.* The UNCOVER Survey: A first-look HST+JWST catalog of 50,000 galaxies near Abell 2744 and beyond. *arXiv e-prints* arXiv:2301.02671 (2023).
60. Brammer, G. *grizli* (2023). URL <https://doi.org/10.5281/zenodo.8210732>. Please cite this software using these metadata.
61. Treu, T. *et al.* The GLASS James Webb Space Telescope Early Release Science Program. I. Survey Design and Release Plans. *arXiv e-prints* arXiv:2206.07978 (2022).
62. Brammer, G. *msaexp*: Nirspec analysis tools (2022). URL <https://doi.org/10.5281/zenodo.7313329>. Please cite this software using these metadata.
63. González-López, J. *et al.* The ALMA Frontier Fields Survey. I. 1.1 mm continuum detections in Abell 2744, MACS J0416.1-2403 and MACS J1149.5+2223. *A&A* **597**, A41 (2017).

64. Zitrin, A. *et al.* Hubble Space Telescope Combined Strong and Weak Lensing Analysis of the CLASH Sample: Mass and Magnification Models and Systematic Uncertainties. *ApJ* **801**, 44 (2015).
65. Pascale, M. *et al.* Unscrambling the Lensed Galaxies in JWST Images behind SMACS 0723. *ApJ* **938**, L6 (2022).
66. Elíasdóttir, Á. *et al.* Where is the matter in the Merging Cluster Abell 2218? *ArXiv e-prints* (2007).
67. Jaffe, W. A simple model for the distribution of light in spherical galaxies. *MNRAS* **202**, 995–999 (1983).
68. Keeton, C. R. A Catalog of Mass Models for Gravitational Lensing. *arXiv e-prints astro-ph/0102341* (2001).
69. Horne, K. An optimal extraction algorithm for CCD spectroscopy. *PASP* **98**, 609–617 (1986).
70. Earl, N. *et al.* *astropy/specutils*: v1.10.0 (2023). URL <https://doi.org/10.5281/zenodo.7803739>.
71. Foreman-Mackey, D., Hogg, D. W., Lang, D. & Goodman, J. emcee: The MCMC Hammer. *PASP* **125**, 306 (2013).
72. Prevot, M. L., Lequeux, J., Maurice, E., Prevot, L. & Rocca-Volmerange, B. The typical interstellar extinction in the Small Magellanic Cloud. *A&A* **132**, 389–392 (1984).

73. Bouchet, P., Lequeux, J., Maurice, E., Prevot, L. & Prevot-Burnichon, M. L. The visible and infrared extinction law and the gas-to-dust ratio in the Small Magellanic Cloud. *A&A* **149**, 330–336 (1985).
74. Calzetti, D. *et al.* The Dust Content and Opacity of Actively Star-forming Galaxies. *ApJ* **533**, 682–695 (2000).
75. Salim, S. & Narayanan, D. The Dust Attenuation Law in Galaxies. *ARA&A* **58**, 529–575 (2020).
76. Korista, K. T. & Goad, M. R. What the Optical Recombination Lines Can Tell Us about the Broad-Line Regions of Active Galactic Nuclei. *ApJ* **606**, 749–762 (2004).
77. Kennicutt, J., Robert C. The Global Schmidt Law in Star-forming Galaxies. *ApJ* **498**, 541–552 (1998).
78. Conroy, C., Gunn, J. E. & White, M. The Propagation of Uncertainties in Stellar Population Synthesis Modeling. I. The Relevance of Uncertain Aspects of Stellar Evolution and the Initial Mass Function to the Derived Physical Properties of Galaxies. *ApJ* **699**, 486–506 (2009).
79. Richards, G. T. *et al.* Spectral Energy Distributions and Multiwavelength Selection of Type 1 Quasars. *ApJS* **166**, 470–497 (2006).
80. Peng, C. Y., Ho, L. C., Impey, C. D. & Rix, H.-W. Detailed Decomposition of Galaxy Images. II. Beyond Axisymmetric Models. *AJ* **139**, 2097–2129 (2010).

81. Pasha, I. & Miller, T. B. pysersic: A Python package for determining galaxy structural properties via Bayesian inference, accelerated with jax. *arXiv e-prints* arXiv:2306.05454 (2023).
82. Atek, H. *et al.* JWST UNCOVER: discovery of $z \lesssim 9$ galaxy candidates behind the lensing cluster Abell 2744. *MNRAS* **524**, 5486–5496 (2023).
83. Sheth, R. K. & Tormen, G. An excursion set model of hierarchical clustering: ellipsoidal collapse and the moving barrier. *MNRAS* **329**, 61–75 (2002).
84. Astropy Collaboration *et al.* Astropy: A community Python package for astronomy. *A&A* **558**, A33 (2013).
85. Price-Whelan, A. M. *et al.* The Astropy Project: Building an Open-science Project and Status of the v2.0 Core Package. *AJ* **156**, 123 (2018).
86. van der Walt, S., Colbert, S. C. & Varoquaux, G. The numpy array: A structure for efficient numerical computation. *Computing in Science Engineering* **13**, 22–30 (2011).
87. Virtanen, P. *et al.* SciPy 1.0: Fundamental Algorithms for Scientific Computing in Python. *Nature Methods* **17**, 261–272 (2020).
88. Hunter, J. D. Matplotlib: A 2d graphics environment. *Computing in Science & Engineering* **9**, 90–95 (2007).
89. Ofek, E. O. MAAT: MATLAB Astronomy and Astrophysics Toolbox. Astrophysics Source Code Library, record ascl:1407.005 (2014). 1407.005.

Data availability The raw JWST data used in this work are publicly available on the Barbara A. Mikulski Archive for Space Telescopes (MAST). These observations specifically are associated with the JWST GO program number 2561, JWST ERS program number 1324, and JWST DD program number 2756. The reduced UNCOVER mosaics, catalogs, lens models as well as spectra are part of the public data release by the UNCOVER team³ 10,19,59. The public ALMA data can be found on the ESO Science Archive under IDs 2018.1.00035.L and 2013.1.00999.S.

Acknowledgements A.Z. acknowledges support by grant 2020750 from the United States-Israel Binational Science Foundation (BSF) and grant 2109066 from the United States National Science Foundation (NSF), and by the Ministry of Science & Technology, Israel. H.A. and I.C. acknowledge support from CNES, focused on the JWST mission, and the Programme National Cosmology and Galaxies (PNCG) of CNRS/INSU with INP and IN2P3, co-funded by CEA and CNES. P.D. acknowledges support from the NWO grant 016.VIDI.189.162 (“ODIN”) and the European Commission’s and University of Groningen’s CO-FUND Rosalind Franklin program. The Cosmic Dawn Center (DAWN) is funded by the Danish National Research Foundation under grant No. 140. Support for the program JWST-GO-2561 was provided through a grant from the STScI under NASA contract NAS 5-03127. This work has received funding from the Swiss State Secretariat for Education, Research and Innovation (SERI) under contract number MB22.00072, as well as from the Swiss National Science Foundation (SNSF) through project grant 200020_207349. Cloud-based data processing and file storage for this work is provided by the AWS Cloud Credits for Research program.

This work is based on observations obtained with the NASA/ESA/CSA JWST, retrieved from the MAST at the *Space Telescope Science Institute* (STScI). STScI is operated by the Association of Universities for

³<https://jwst-uncover.github.io>

Research in Astronomy, Inc. under NASA contract NAS 5-26555. This work is also based on observations made with ESO Telescopes at the La Silla Paranal Observatory and the *Atacama Large Millimeter/submillimeter Array* (ALMA), obtained from the ESO Science Archive facility. ALMA is a partnership of ESO (representing its member states), NSF (USA) and NINS (Japan), together with NRC (Canada), MOST and ASIAA (Taiwan), and KASI (Republic of Korea), in cooperation with the Republic of Chile. The Joint ALMA Observatory is operated by ESO, AUI/NRAO and NAOJ. The National Radio Astronomy Observatory (NRAO) is a facility of the NSF operated under cooperative agreement by Associated Universities Inc.

This research made use of `Astropy`,⁴ a community-developed core Python package for Astronomy^{84,85} as well as the packages `NumPy`⁸⁶, `SciPy`⁸⁷, `Matplotlib`⁸⁸ and the MAAT Astronomy and Astrophysics tools for `MATLAB`⁸⁹.

Author contributions A.Z., J.E.G., and L.J.F. wrote the manuscript. L.J.F. made the figures. L.J.F. and I.L. performed the line fits. I.L. designed the program and produced the deep spectrum. R.B. and I.L. reduced the data. L.J.F. and A.Z. constructed the lens model. P.D. provided simulations to contextualise the observational results obtained. V.K. and I.L. measured emission line strengths. I.C. ran the completeness simulations. T.B.M., D.S. and E.N. measured the source size. I.L. and R.B. are the PIs of the UNCOVER program. All authors contributed to the manuscript and aided the analysis and interpretation.

Competing Interests The authors declare no competing financial interests.

Additional information

Reprints and permissions information is available at www.nature.com/reprints.

⁴<http://www.astropy.org>